Epitranscriptome Mapping of m^{6}A RNA Modifications in Glioma Tumor Tissue

Syeda Maheen Batool[1*], Saad Murtaza Khan[1*], Koushik Muralidharan[1*], Ana K. Escobedo[1], Hanna Lee[1], Emil Ekanyake[1], Tiffaney Hsia[1], Bob S. Carter[1], Leonora Balaj[1]

[1]Department of Neurosurgery, Massachusetts General Hospital, Harvard Medical School, Boston, MA, USA. [*]co-first authors

Corresponding author: Email: Balaj.leonora@mgh.harvard.edu Adresss:185 Cambridge St. Boston, MA 02114

Abstract

Glioma represents the most common primary central nervous system (CNS) neoplasm in adults. IDH1 mutation is recognized as a hallmark alteration with important diagnostic and prognostic implications. There is considerable evidence for global DNA hypermethylation induced secondary to IDH mutation. However, there is limited understanding of the RNA methylation patterns and its role in glioma biology. In this study, we performed transcriptome wide profiling of N6-methyladenosine (m^{6}A) modifications across IDH mutant (n = 8) and wild-type (n = 7) gliomas using Oxford Nanopore Technologies' direct RNA sequencing platform. Our approach enabled high-depth coverage of native transcripts, revealing nearly twice as many full-length transcripts in IDH mutant gliomas compared to wild-type. Notable differences in alternative splicing were observed across glioma subtypes, with truncated and non-coding isoforms more prevalent in glioblastoma (GBM). We further identified significant changes in isoform usage within key metabolic (NAMPT, PKM) and immune (CD63, CD151, CD81) pathways. Chromosomal distribution of m^{6}A sites showed a higher prevalence of m^{6}A modifications in IDH mutant gliomas, with the most pronounced differences on chromosomes 19 and 16. Further stratification by TERT, MGMT, and TP53 mutations revealed similar patterns of increased m6A site numbers in mutant groups, highlighting the importance of integrating epigenomic and epitranscriptomic data in glioma research. These findings highlight the role of m^{6}A modifications in the metabolic reprogramming unique to IDH mutant gliomas, providing insights into potential mechanisms of tumorigenesis and therapeutic resistance.

Introduction

Glioma represents the most common primary central nervous system (CNS) neoplasm in adults, with an average annual age-adjusted incidence rate (AAAIR) of 6 per 100,000 population[1,2]. IDH1 mutation is recognized as a hallmark alteration prevalent in >80% of WHO grade II/III gliomas[3], >70% of Secondary Glioblastoma (GBM)[4], and <10% of Primary GBM[5] (all previous IDH1 mutant GBM lesions are now classified as Grade 4, Astrocytoma). Furthermore, clinical studies have established this mutation as a key diagnostic and prognostic biomarker[6]. These findings have led to reclassification of gliomas (WHO 2021)[7], underscoring the favorable prognosis and improved overall survival of the IDH mutant gliomas compared to the more aggressive clinical course seen in IDH1-wild-type gliomas[8,9].

Isocitrate dehydrogenase (IDH) enzyme plays an essential role in several metabolic processes, including the Krebs cycle, glutamine metabolism, lipid synthesis, and redox reactions[10]. IDH1 and IDH2 localize to the mitochondrial matrix whereas IDH1 is located in the cytoplasm and peroxisomes[10]. The enzyme's catalytic activity facilitates conversion of isocitrate into α-ketoglutarate (α-KG)[10]. Oncogenic IDH mutation, specifically IDH1.R132H (CGT>CAT at nucleotide position 395 in codon 132) alters the arginine residue, crucial for the catalytic activity[11–13]. The resulting mutant IDH enzyme exhibits decreased affinity for isocitrate, and an increased affinity for NADPH. This unique interplay leads to the conversion of α-KG into D-2-hydroxyglutarate (2HG), employing NADPH as a cofactor[104].

2HG, identified as an oncometabolite in IDH mutant gliomas has been described in relation to tumor cellularity, tumorigenesis, and overall survival[14]. At the molecular level, 2HG also exerts an epigenetic influence, regulating methylation of cytosine residues in DNA and lysine residues in histone proteins[15]. More recently, Elkashef et al described 2HG's role in increasing global N6-methyladenosine (m^6A) RNA modifications through direct inhibition of fat mass and obesity associated protein (FTO) activity, a known m^6A eraser[16]. This change in RNA methylation levels in turn promotes antitumor activity of acute myeloid leukemia cells driven by inhibition of downstream proliferation pathways[16]. While genomic hypermethylation has been well described in IDH mutant gliomas, there is a limited understanding of the RNA methylation and transcription patterns[17]. This could provide insights into the unique role of IDH mutation as a favorable prognostic factor in gliomas, a correlation not observed in other IDH mutant malignancies (melanoma, cholangiocarcinoma, cartilaginous tumors)[17].

There are over 163 characterized RNA modifications, with methylation of adenosine at position N6, (m^6A) identified as one of the most prevalent modification in different types of RNAs (mRNA, tRNA, rRNA, circRNA, miRNA, lncRNA)[18,19]. Three distinct groups of binding proteins, widely known as "m6A regulators" induce change in m^6A RNA expression: readers; detect base alteration, writers; catalyze or deposit, and erasers; remove the alteration[20,21].

Here, we investigated the methylome and transcriptome of gliomas stratified by IDH status (mutant vs. wild-type). Our workflow utilizes the direct RNA sequencing platform of Oxford Nanopore Technologies (ONT) to detect and map m^6A sites at single nucleotide resolution in tumor tissue derived RNA.

Results

Overview of the experimental workflow and quality control metrics.

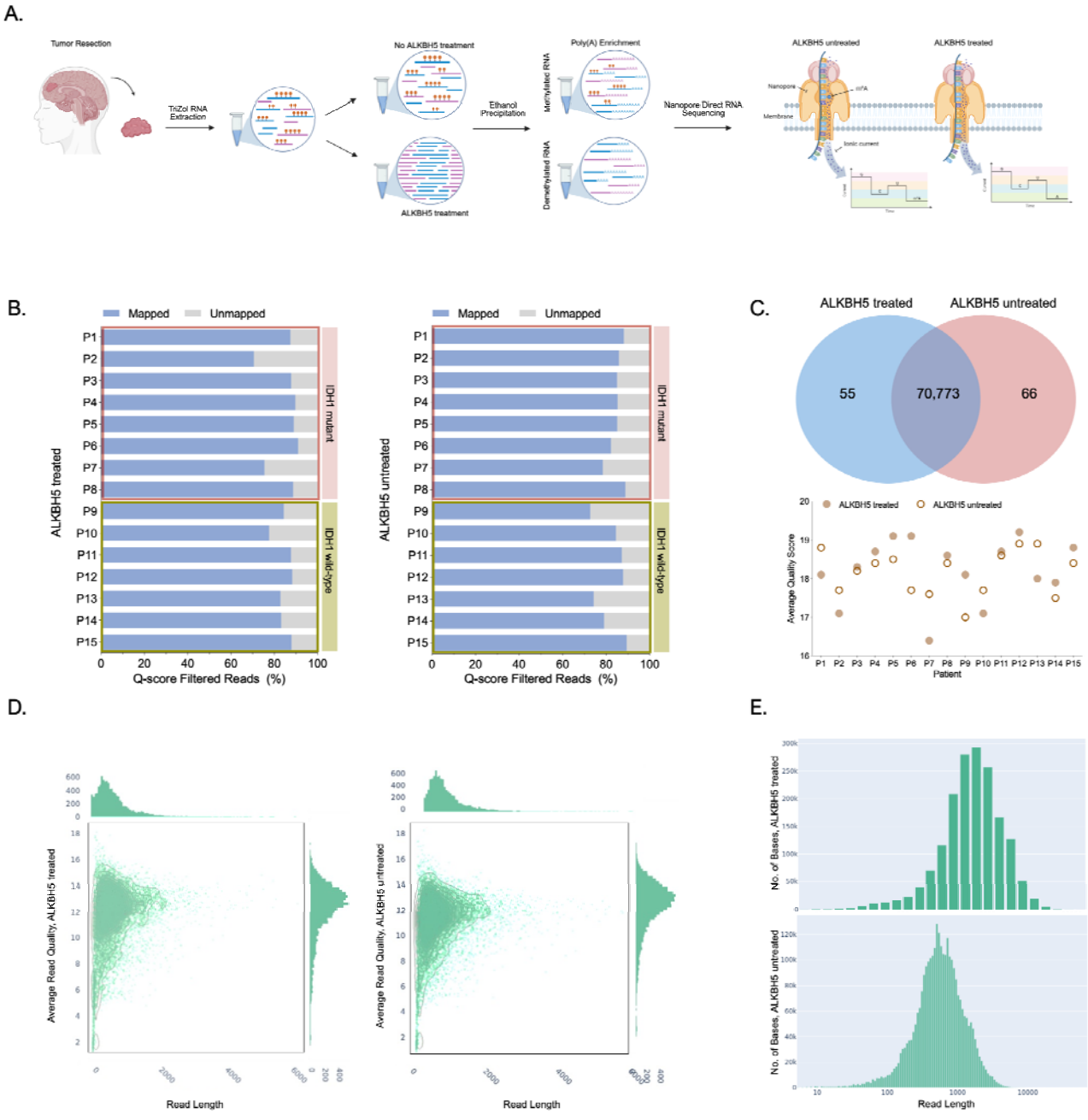

The experimental workflow (**Fig. 1a**) was designed to allow RNA sequencing of tumor tissue derived RNA using the Nanopore Direct RNA Sequencing platform (**see Methods)**. Total, full length RNA was extracted from flash-frozen tumor tissue and subjected to demethylation (along with mock treatment) using recombinant m^6A demethylase (ALKBH5). ALKBH5 treated and untreated full-length RNA was repurified and poly(A) enriched, prior to library preparation (**Fig. 1a, see Methods**). Following optimization of the sequencing approach, the protocol was implemented in tumor tissue across the study cohort (N = 15) comprising IDH1 mutant (n = 8, P1-P8) and IDH1 wild-type (n = 7, P9-P15) gliomas (**Fig. 1a, Supplementary Figure 2a**).

Removal of m^6A from tumor RNA was confirmed using an antibody-based quantitative ELISA (**Supplementary Figure 1a**). In total RNA, ALKBH5 untreated sample had a 3.5 fold higher (Student's one-tailed t-test, p = 0.0001,***) mean m^6A abundance than the demethylated (ALKBH5 treated) sample (mock: 0.136 ± 0.004%, ALKBH5 KD: 0.045 ± 0.003%, **Supplementary Figure 1a, left panel**). The quantitative confirmation of m^6A demethylation treatment was also extended to poly(A) enriched RNA (**Supplementary Figure 1a, right panel**). Consistent with previous observations, results demonstrated a 1.4 fold higher (Student's one-tailed t-test, p = 0.0471,*) mean m^6A abundance in ALKBH5 untreated (0.03 ± 0.003%) RNA as compared to treated RNA (0.02 ± 0.004%) (**Supplementary Figure 1a, right panel)**.

Initial data processing consisted of rigorous testing to compare the sequencing output from ALKBH5 treated and untreated RNA. Overall, in ALKBH5 untreated RNA, the number of quality score (Q-score) filtered reads varied from a minimum of 39,039 reads to a maximum 1,126,075 reads (Mean ± SEM; 316,595 ± 70,188) (**Supplementary Figure 2c, bottom panel**). In ALKBH5 treated RNA, the number of Q-score filtered reads varied from a minimum of 29,076 reads to a maximum of 698,444 reads (Mean ± SEM; 264,185 ± 51,526) (**Supplementary Figure 2c, top panel**). The difference (Δ = 52,410) noted in the average number of reads between the treated vs. untreated RNA was not statistically significant (p = 0.2859, Student's two-tailed paired t-test) (**Supplementary Figure 2c**). In the ALKBH5 treated (**Fig. 1b, left panel**) RNA samples, on average 84.8% reads were mapped (70.6-91.0%). Similar mapping rate was observed for the paired untreated (**Fig. 1b, right panel**) samples (Mean ± SEM; 83.6% ± 1.5%). Overall, IDH1 status was not associated with any significant effect on the distribution of mapped reads in ALKBH5 treated (mut vs wt; 84.96 vs 84.58, p = 0.9062) and untreated RNA (mut vs wt; 84.84 vs 82.18, p = 0.3307) (**Fig. 1b**). Comparison of the detected genes across treated and untreated RNA yielded a 99% (70,773) shared signature (**Fig. 1c, top panel**).

Average quality scores were compared in paired treated and untreated RNA across the study cohort (**Fig. 1c, bottom panel**). Finally, combining all samples (n = 15) we compared the per sequence quality (log transformed read length vs. average read quality) in ALKBH5 treated (**Fig. 1d, left panel**) and untreated (**Fig. 1d, right panel**) RNA. The kernel density estimation plots yielded similar distribution with majority reads having a Q score of ≥ 10. Additionally, log transformed read lengths were plotted for treated and untreated RNA (**Fig. 1e**).

Finally, mean read depth coverage was quantified in ALKBH5 treated and untreated samples across the different transcript regions (5'UTR, CDS, 3'UTR) (**Supplementary Figure 2b**). The CDS region demonstrated the highest mean read depth coverage for both sample types in IDH1 mutant and wild-type groups (**Supplementary Figure 2b**). The 3'UTR region had lower read depth coverage compared to the CDS region, but higher mean read depth than the 5'UTR region (**Supplementary Figure 2b**).

RNA Biotype Distribution and Full-Length Transcript Prevalence Analysis.

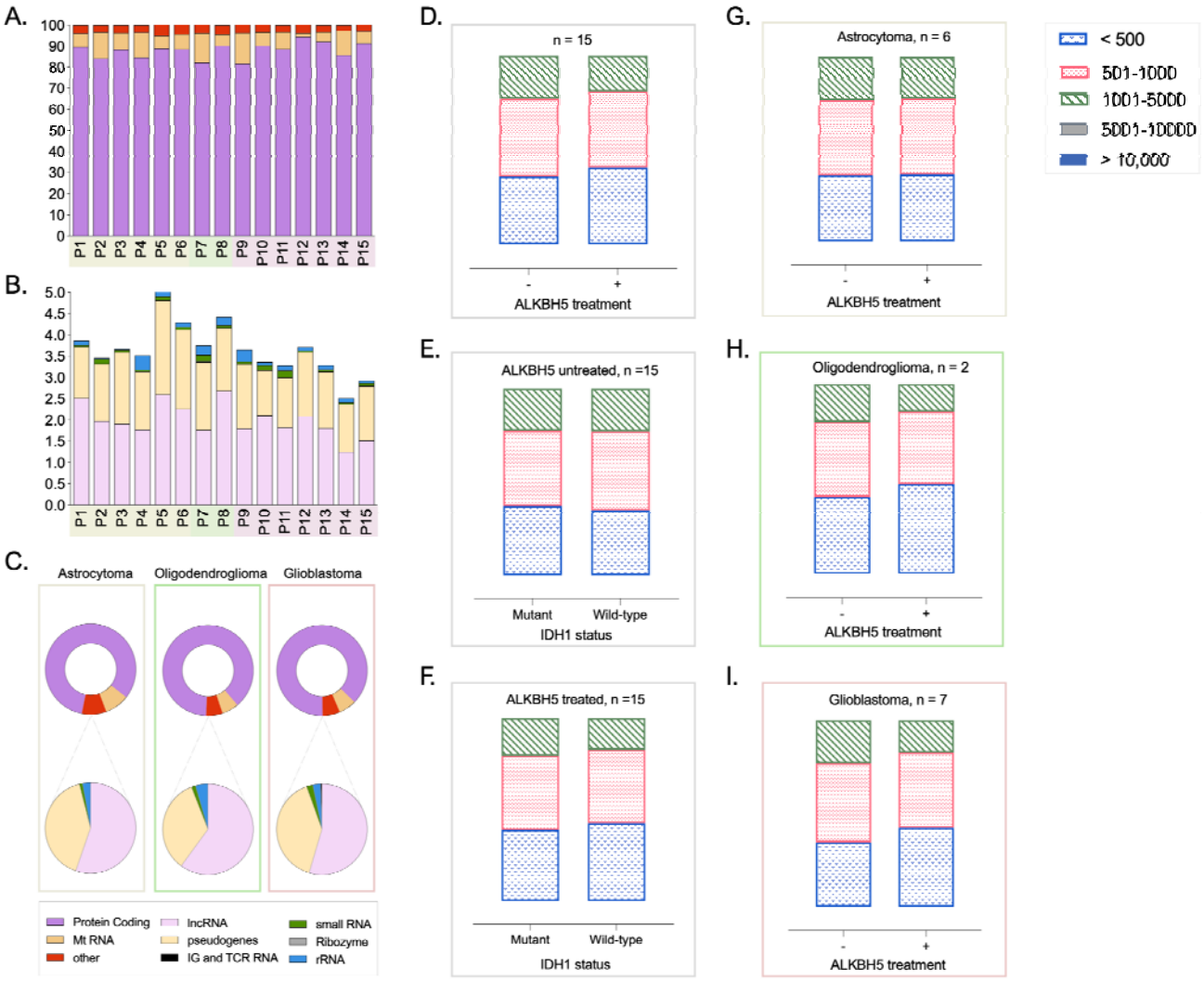

Following quality control testing we quantified the RNA biotypes in the study cohort stratified by IDH1 status and clonal subtype (**Fig. 2a-c**) and expressed as fractional abundance. As previously reported, protein coding RNA was the most prevalent biotype (84.16% - 94.51%) across all individual samples (n = 15, **Fig. 2a**). Successful poly(A)+ isolation was confirmed with less than 0.4%

ribosomal RNA detected (**Fig. 2b**). A closer look at the non-protein coding biotypes across the patients (**Fig. 2b**) demonstrated variation in the mitochondrial RNA (Mt RNA) prevalence. To investigate this further, we grouped the patients into the distinct clonal subtypes: astrocytoma (n = 6), oligodendroglioma (n = 2), and glioblastoma (GBM; n = 7) (**Fig. 2c**). Highest prevalence of Mt RNA was observed in Astrocytomas (8.76%) followed by GBM (6.26%) and Oligodendrogliomas (5.95%) (**Fig. 2c**). Interestingly, the IDH wild-type group (GBM) had the lowest prevalence of lncRNA (1.72%). On the other hand, both astrocytomas and oligodendrogliomas had very similar but higher abundance of detected lncRNA (astrocytoma: 2.21%, oligodendroglioma: 2.62%) (**Fig. 2c**).

Nanopore RNA sequencing platform offers a unique opportunity for full-length RNA transcripts discovery and quantification. We explored full-length transcripts across different conditions using Bambu[22] (**see Methods**) (**Fig. 2d-i**). A comparison of ALKBH5 treated compared to untreated samples (**Fig. 2d**) isolated a higher prevalence of shorter (< 500 bp) transcripts in the treated RNA (40.63% vs. 35.89% in untreated). Similar difference was also observed in the transcripts ranging from 1,001-5,000 bp in length with more enrichment in untreated (22.7%) vs. treated RNA (19.05%) (**Fig. 2d**). Further stratification of ALKBH5 treated (**Fig. 2f**) and untreated (**Fig. 2e**) samples by IDH1 status also highlighted differences in the distribution of RNA length. Interestingly, a shift was seen in the IDH wild-type treated RNA with higher (42.50%) prevalence of shorter (< 500 bp) transcripts than the mutant group (38.99%) (**Fig. 2f**). However, this difference was not seen in the untreated RNA (**Fig. 2e**).

Next, we directly compared the treated and untreated RNA across the clonal subtypes (**Fig. 2g-i**). Interestingly, in astrocytomas the overall distribution was very similar across both conditions with 76.7% transcripts ≤ 1,000 bp in untreated RNA and 77.4% transcripts ≤ 1,000 bp in treated RNA (**Fig. 2g**). However, larger differences were noted in oligodendroglioma and GBM groups. Specifically, ALKBH5 treated RNA in oligodendroglioma lead to enrichment (85.3%) of shorter (≤ 1,000 bp) full-length transcripts when compared to untreated RNA (80.0%) (**Fig. 2h**). Similar trend was also reported in the GBM group with 82.7% transcripts ≤ 1,000 bp in the treated RNA vs. 77.0% in untreated RNA.

The overall analysis of RNA biotypes and full-length transcripts distribution demonstrated differences across the IDH clonal subtypes with variation in prevalence of Mt RNA and enrichment of shorter transcripts across treated and untreated RNA.

Global gene expression analysis and identification of characteristic markers.

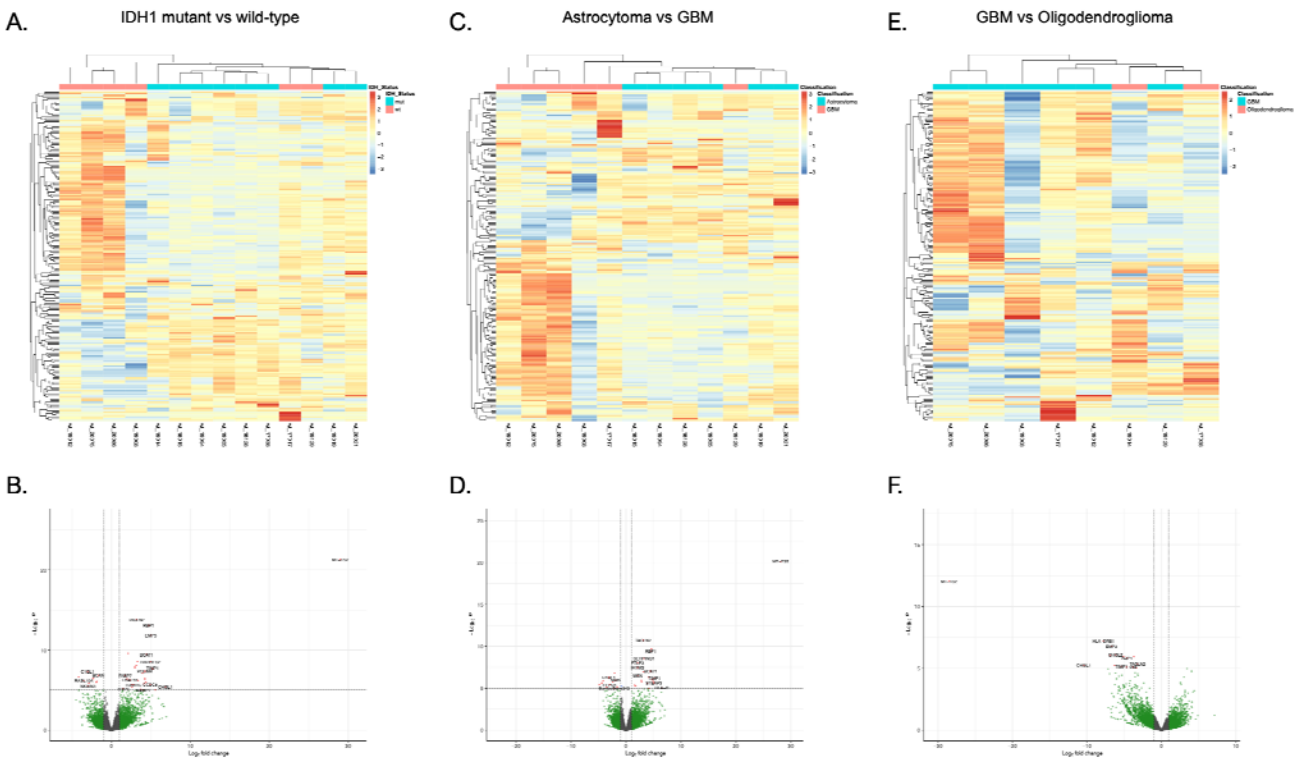

We performed a comparative gene expression (**Fig. 3a, c, e**) and differential expression (**Fig. 3b, d, f**) analysis across three distinct comparison groups: (i) IDH1 mutant vs. wild-type (**Fig. 3a-b**), (ii) Astrocytoma vs. GBM (**Fig. 3c-d**), and (iii) GBM vs. Oligodendroglioma (**Fig. 3e-f**). Gene expression analysis was performed using variance stabilized transformed (VST) normalized gene expression (see **Methods**), while DESeq2 was utilized for differential expression analysis (see **Methods**).

Clear clustering of samples was observed across all three comparisons (**Fig. 3a, c, e**) with distinct expression patterns in gene subsets. In astrocytoma vs. GBM comparison we observed more heterogeneous expression patterns with more variation seen in individual patients (**Fig. 3b)**. Statistically significant upregulated and downregulated genes were identified for each comparison (**Fig. 3b, d, f**): (i) IDH1 mutant vs. wild-type (**Fig. 3b;** 131 up- and 68 down- regulated), (ii)

Astrocytoma vs. GBM (**Fig. 3d;** 90 up- and 43 down- regulated), (iii) GBM vs. Oligodendroglioma (**Fig. 3f;** 5 up- and 43 down- regulated).

RNA transcript isoform diversity and alternative splicing across IDH mutant and wild-type gliomas.

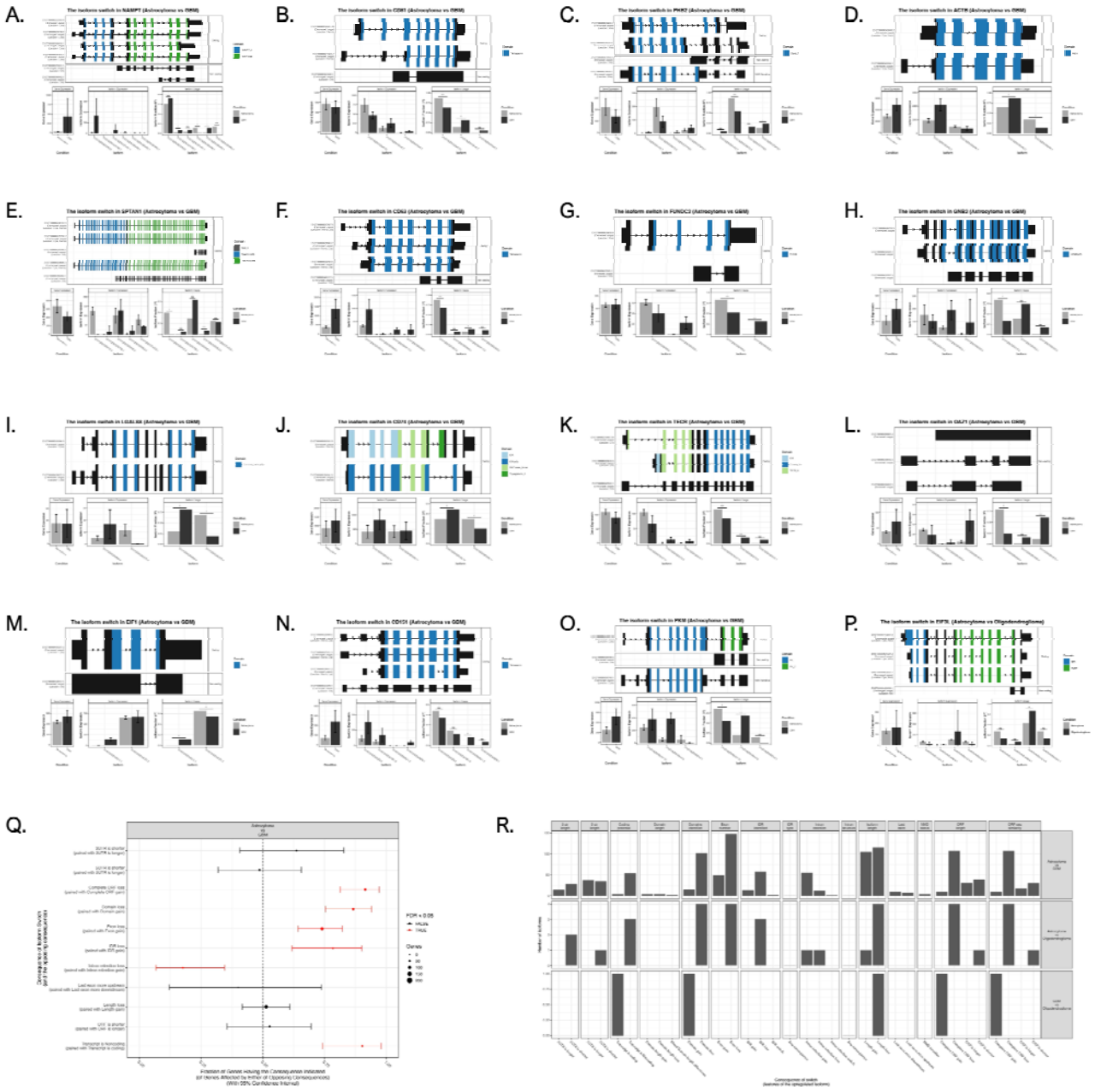

Changes in the proportion of each isoform with varying biotypes can contribute to gene expression. We examined this in our study cohort by using a multifaceted approach encompassing gene expression, differential isoform expression (DIE), and differential isoform usage (DIU) analysis (IsoformSwitchAnalyzeR, **see Methods**). We found 32 isoforms encoded by 20 genes with

differential usage between the clinical groups. IDH1 status itself did not yield any significant switches. However, clonal subtype analysis identified a total of 25 statistically significant isoform switches: astrocytoma vs. GBM (n = 23), and astrocytoma vs. oligodendroglioma (n = 2).

Based on the downstream functional role, we further characterized the genes into distinct categories (**Fig. 2a-p**): autophagy and cell fate (NAMPT, SPTAN1, LGALS8), protein synthesis and trafficking (EIF1, OAZ1, EIF3L), immune cell and inflammation (CD81, CD63, CD74, CD151), lipid and cholesterol metabolism (FUNDC2, TECR, PKM, ACTB), signaling and intercellular communication (PHB2, GNB2).

In the autophagy and cell fate group, increased usage of protein coding isoform (NAMPT-201) and corresponding high NAMPT expression was noted in GBM (**Fig. 2a**). SPTAN1 was more highly expressed in astrocytoma (**Fig. 2e**). Low expression in GBM was associated with decreased usage of protein coding SPTAN-201 and increased usage of non-protein coding (retained intron) SPTAN-211 (**Fig. 2e**). Similar gene expression of LGALS8 but increased usage of the protein-coding isoform was observed in GBM compared to astrocytoma (**Fig. 2i**).

Majority of the immune cell and inflammatory markers (CD63, CD74, CD151) were shown to be upregulated in GBM (**Fig. 2f, j, n**) with CD81 expressed at similar levels across the clonal subtypes (**Fig. 2b**). Isoform switching in this functional group was most notably observed in the protein coding isoforms. Specifically, shorter protein coding isoforms (CD81-205, CD63-214, CD151-213) demonstrated increased usage in GBM compared to decreased usage of longer isoforms (CD81-201, CD63-201) (**Fig. 2b, f, j, n**).

In protein synthesis and trafficking group even though EIF1 was similarly expressed in astrocytoma vs GBM, increased usage of non coding and decreased usage of protein coding isoforms was seen in GBM (**Fig. 2m**). Similarly, EIF3L was expressed at similar levels (**Fig. 2p**) in astrocytoma and oligodendroglioma with increased usage of protein coding EIF3L-215 in the oligodendroglioma group (**Fig. 2p**). However, Another gene, OAZ1 was seen to be highly expressed in GBM with significantly decreased usage of non-coding OAZ1-203 (1 exon, 2,832 bp) and increased usage of non-coding OAZ1-210 (3 exons, 1,357 bp) (**Fig. 2l**).

From the genes in the lipid and cholesterol metabolism category, PKM (**Fig. 2o**) and ACTB (**Fig. 2d**) expression was higher in GBM, whereas similar expression was observed for TECR (**Fig. 2k**) and FUNDC2 (**Fig. 2g**). Higher expression of PKM in GBM was associated with increased usage of non-coding PKM-211 and decreased usage of protein coding PKM-202 (**Fig. 2o**). Similar trend was also noted for FUNDC2, with increased usage of non-coding FUNDC2-207 and decreased usage of protein coding FUNDC2-201 (**Fig. 2o**). Interestingly, for TECR (**Fig. 2k**) and ACTB (**Fig. 2d**), preferential increased usage of protein coding isoforms with fewer exons (TECR-207; 12 exons, ACTB-213; 5 exons) was seen in GBM compared to protein coding isoforms with greater number of exons (TECR-201; 13 exons, ACTB-217; 6 exons) (**Fig. 2d, k**).

Low PHB2 expression in GBM was associated with decreased usage of protein coding PHB2-203 and increased usage of non-coding PHB2-205 isoforms (**Fig. 2o**). Conversely, high expression of GNB2 in GNB2 was associated with decreased usage of longer protein coding GNB2-201 (1,664 bp) and increased usage of shorter protein coding (GNB2-202; 1,524 bp) and non-coding (GNB2-211; 1,702 bp) isoforms (**Fig. 2h**).

Given the variation in isoform switching driven by either the isoform biotype and/or transcript structure (length, exon density) we quantified the statistical significance of observed differences in the form of consequence plots (see Methods) (**Fig. 2q-r**). The most remarkable features common to isoforms with increased usage in GBM include: (i) shorter 3'UTR length, (ii) non-coding biotype, (iii) complete open reading frame (ORF) loss, (iv) domain loss, (v) exon loss, and (vi) intrinsically disordered region (IDR) loss (**Fig. 2q-r**).

Profiling m^{6}A distribution and functional ecosystem in IDH mutant gliomas.

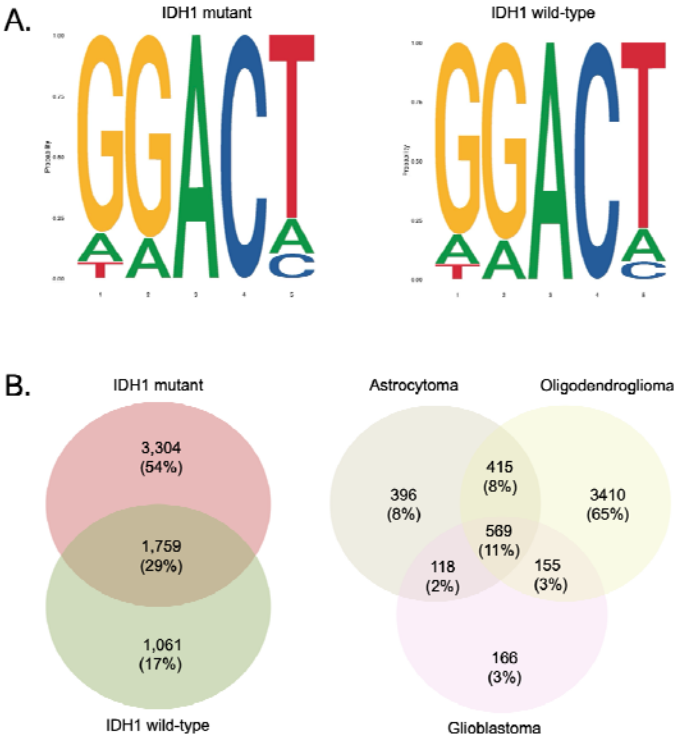

In our analysis of glioma tumor tissue, we identified a significant number of m^{6}A motifs (probability score ≥ 0.9), categorized into DRACH (D = A/G/U, R = A/G, A = m^{6}A, C = C) motifs (**Fig. 5a**). No differences were observed in the nucleotide composition and probability distribution of the DRACH motifs stratified by IDH1 status (IDH1 mutant; **Fig. 5a, left panel,** IDH1 wild-type; **Fig. 5a, right panel**). Overall, the DRACH motif, characterized by the sequence DRA*CH (where * denotes m^{6}A site), demonstrated a high probability of occurrence for the nucleotides 'G' at positions 1 and 2, 'A' at positions 3 and 5, and 'C' at position 4 (**Fig. 5a**). This motif is consistent with the canonical DRACH sequence known to be enriched in m^{6}A sites.

Quantification of the overall number of m^{6}A sites detected across the clinical groups demonstrated an overlap of only 29% (n = 1,759) between IDH1 mutant and wild-type groups (**Fig. 5b, left panel**). More than 50% (n = 3,304) of the m^{6}A sites detected were found to be unique to the IDH1 mutant group (**Fig. 5b, left panel**). A comparative distribution analysis across the distinct clonal subtypes (**Fig. 5b, right panel**) also further highlighted the enrichment of m^{6}A sites in oligodendroglioma (65%, n = 3,410 sites) followed by astrocytoma (8%, n = 396 sites), and GBM (3%, n = 166 sites) (**Fig. 5b, right panel**).

Next, we investigated the prevalence of m^{6}A sites across various RNA biotypes (**Fig. 5c**) in the IDH1 mutant (**Fig. 5c, left panel**) and IDH1 wild-type (**Fig. 5c, right panel**) study population. The highest prevalence of m^{6}A modifications was observed in protein coding mRNA (IDH1 mutant: 77.1%, IDH1 wild-type: 76.17%) followed by retained intron (IDH1 mutant: 10.25%, IDH1 wild-type: 11.36%) and nonsense mediated decay (NMD) biotypes

(IDH1 mutant: 7.70%, IDH1 wild-type: 8.6%) (**Fig. 5c**). Larger differences were observed in the prevalence of m^{6}A sites across 'other' RNA biotypes between IDH1 mutant (2.10%) vs wild-type (1.05%) group: (i) higher prevalence of m^{6}A modified lncRNA in IDH1 mutant group (1.82% vs. 0.83%), (ii) higher prevalence of unannotated (novel) transcripts in IDH1 mutant group (0.05% vs. 0.0%), (iii) higher prevalence of m^{6}A modified pseudogenes in IDH1 mutant group (0.16% vs. 0.07%), (iv) higher prevalence of m^{6}A modified Mt rRNA in IDH1 wild-type group (0.06% vs. 0.05%) (**Fig. 5c**).

A comparative analysis of m^{6}A transcriptome distribution demonstrated distinct patterns across the RNA biotypes (**Fig. 5d**). The analysis was performed with patients stratified by IDH1 status (mutant vs. wild-type). Protein coding RNA groups exhibited a bimodal distribution, with peaks at the CDS (near the stop codon) and 3'UTR region (**Fig. 5d**). A bimodal distribution was also observed in the retained intron group, with a higher concentration of m^{6}A sites in 5'UTR. and 3'UTR regions. Nonsense mediated decay (NMD) RNA transcripts demonstrated a single prominent peak in the 3'UTR region (**Fig. 5d**). No significant differences were observed between the clinical groups across (**Fig. 5d**).

Chromosomal distribution of m^{6}A sites across clinical groups.

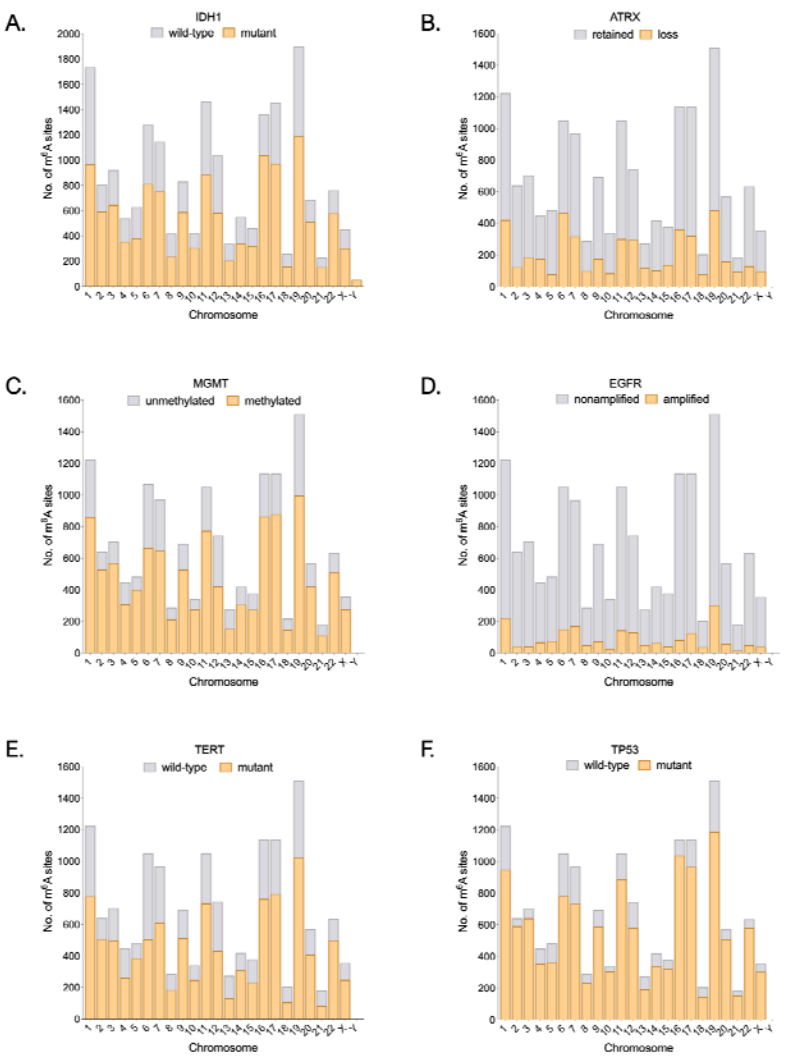

Chromosomal (Ch) distribution of the detected m^{6}A sites revealed significant variability across the IDH1 mutant and wild-type groups (**Fig. 6a**). Interestingly, targets in the IDH1 mutant group were localized most frequently to Ch 19 (n = 1190), followed by Ch 16 (n = 1039) and 17 (973) (**Fig. 6a**). On the contrary, the sites most likely to be modified in the IDH1 wild-type group were localized to Ch 1 (n = 770), followed by Ch 19 (n = 711) and 11 (579) (**Fig. 6a**). Overall, not only higher number of targets were modified per chromosome in the IDH1 mutant group but the chromosomes with the largest discrepancy (Δ = mut - wild-type) between the two glioma subtypes were Ch 16 (Δ =714), Ch 17 (Δ = 489), and Ch 19 (Δ = 479) (**Fig. 6a**).

Similar to IDH, three other molecular alterations demonstrated higher enrichment of m^{6}A sites across all chromosomes in the mutant group: MGMT methylation (**Fig. 6c**), TERT promoter mutation (**Fig. 6e**), and TP53

mutation (**Fig. 6f**). EGFR amplification (a common alteration in GBM) was associated with very few m^6A sites, with more modified targets seen in the wild-type group (**Fig. 6d**). ATRX loss also had similar loss of m^6A sites, with higher abundance in ATRX retained group (**Fig. 6b**).

Discussion

In this study, we performed transcriptome wide profiling of m^6A modifications across IDH mutant and wild-type gliomas. Our workflow leveraged the direct RNA sequencing platform of ONT, enabling sensitive, high-depth coverage of native transcripts derived from tumor tissue RNA[23]. Downstream analysis was tailored to allow a multifaceted comparison of isolated RNA and is described below.

We used Bambu[22] to map full-length transcripts of varying lengths (<500 bp - >10,000 bp). Of the 4,089,398 mapped RNA reads, 32.65% (1,335,000) were full-length transcripts. Notably, we observed almost a two-fold greater number of full-length transcripts in IDH mutant gliomas (n = 860,053) compared to wild-type (n = 474,947) gliomas. Furthermore, differences in proportion of full-length transcripts were observed across clonal subtypes: astrocytoma (40.7%0, oligodendroglioma (23.74%), and GBM (35.58%).

Next, we compared the read length distributions of full-length transcripts. While the overall read length distributions were similar in IDH mutant and wild-type groups, subtype analysis revealed a higher prevalence of shorter transcripts in GBM and Oligodendroglioma, particularly in ALKBH5 treated vs. untreated samples. It is important to note that our study included only two patients with oligodendroglioma, which highlights the need for further investigation in larger cohorts. A closer look at the RNA biotypes demonstrated the highest prevalence of Mt RNA in astrocytomas. Additionally, both astrocytomas and oligodendrogliomas exhibited a higher prevalence of detected lncRNA compared to GBM.

Isoform analysis has garnered significant interest in recent studies, given the advances in detection and prediction. In the context of IDH mutant gliomas, we were particularly interested in correlating alternative splicing with gene expression using IsoformSwitchAnalyzeR[24]. Previous literature has provided evidence of the metabolic reprogramming of gliomas secondary to IDH mutation. This in turn is mediated due to alteration of key biological pathways: lipid and cholesterol synthesis[25,26], cell to cell signaling[25], autophagy[27], and immune response[28,29]. To better understand these functional consequences, we analyzed isoform switches in transcripts grouped by functional categories. Nicotinamide phosphoribosyltransferase (NAMPT) is a key enzyme that maintains nicotinamide adenine dinucleotide (NAD) levels in cancer cells. High NAMPT levels in GBM have been correlated with poor survival and increased tumorigenesis[30]. We observed higher NAMPT expression in GBM compared to astrocytoma, with significantly higher usage of the protein-coding isoform NAMPT-201 in GBM. Similarly, Pyruvate kinase M2 (PKM2), an enzyme that catalyzing the final step of glycolysis, has been associated with poor survival in GBM[30,31]. Our findings are consistent, showing higher PKM2 expression in GBM. However, this was linked to increased usage of non-coding PKM-211 isoform and decreased usage of protein coding PKM-202 isoform.

We also identified common characteristics of isoforms preferentially used in GBM: exon loss, IDR loss, shorter 3'UTR, and ORF loss. This in combination with earlier observation of higher proportion of short (<500 bp) transcripts and lower counts of full-length transcripts in GBM raises an important question in tumor progression. It is possible that GBM cells rely on truncated, shorter isoforms to

evade immune control and enhance tumor metabolism, thereby promoting tumor proliferation. This is supported by our findings of increased usage of shorter protein coding isoforms in GBM when examining the immune response markers (CD63, CD151, CD81). However, all immune markers were upregulated (high expression) in the GBM group. This aligns with previous studies reporting suppression of terminal cell differentiation and immune response in IDH mutant cancers[17]. We hypothesize that isoform switches resulting in truncated proteins may correlate with a more aggressive tumor phenotype[32]. Functional validation studies are needed to explore the clinical implications of these events and their potential role in treatment resistance.

For identification of m^6A modified nucleotides, we employed m6Anet[23], a neural-network-based multiple instance learning (MIL) model framework. A key advantage of this computational method is its ability to quantify single molecule modification probability from a single sample. This represents a major shift from previous comparative approaches[23]. Consistent with our hypothesis, a direct comparison of glioma subtypes demonstrated an overlap of only 29% of m^6A sites between IDH mutant and wild-type groups. Over 50% of detected sites were unique to the IDH mutant group. IDH1/2 mutations are known to induce a DNA hypermethylator phenotype when compared to wild-type counterparts. However, recently Pianka et al. used methylation RNA immunoprecipitation sequencing (MeRIP-seq) RNA sequencing to explore RNA methylation in IDH mutant gliomas[33]. The study reports 2HG mediated hypermethylation. Here, we extend these findings to the m^6A RNA methylome using the Nanopore platform[34].

A chromosomal distribution analysis of m^6A modifications revealed a much higher prevalence of m6A targets across all chromosomes in the IDH mutant glioma group. The greatest difference (Δ = mut - wild-type) was seen on chromosomes 19 and 16, with lower differences on chromosomes 5, 14, 12, 21, and 18. According to a study that has looked at the chromosomal patterns of DNA methylation, hypermethylated gene bodies were localized to chromosomes 16 and 13 (among others) with lowest hypermethylation ratio seen in chromosomes 5 and 18[33]. Our study provides similar insights, but in the context of RNA modifications. We further stratified our chromosomal distribution analysis by hallmark glioma alterations, including TERT, MGMT, and TP53 mutations, all of which demonstrated higher numbers of m6A sites in the mutant group. This underscores the importance of parallel profiling of epigenomic and epitranscriptomic patterns which may hint to important biological consequences.

Lastly, examining the biotypes of m^6A modified RNAs, identified showed no differences in the protein coding RNA. However, lncRNA was not only more prevalent in IDH mutant gliomas but also more frequently modified. In contrast, mitochondrial rRNA was more prevalent in the IDH mutant group but more frequently modified in the IDH wild-type group. These findings highlight the complex interplay of RNA modifications in glioma biology and warrant further investigation.

Finally, examining the biotypes of targets identified showed no differences in the protein coding RNA. However, lncRNA was not only more prevalent in IDH mutant gliomas but also more frequently modified. On the contrary, Mt rRNA was seen to be more prevalent in the IDH mutant group. However, this specific RNA subtype was more frequently modified in the iDH wild-type group.

Methods

Study Population

The study population (n=15) included patients 18 years or older with histopathologically confirmed IDH1 mutant or wildtype gliomas who underwent surgery at Massachusetts General Hospital (MGH) for biopsy or resection of a primary brain lesion. The study population can be classified into high-grade glioma (HGG) (III/IV) and low-grade glioma (LGG) (I/II) groups, with varying IDH1 status as follows: 1) IDH1 R132H, HGG (n=4), 2) IDH1 WT, HGG (n=4), 3) IDH1 R132H, LGG (n=4), 4) IDH1 WT, LGG (n=4). Exclusion criteria for the cohort included history of primary or metastatic cancers, active infectious disease (including SARS-CoV-2), and enrollment in clinical trials. All samples were collected with informed consent under Partners institutional review board (IRB)-approved protocol 2017P001581. Patient demographics are and clinical details are depicted in oncoprint format in **Supplementary Figure 2a**.

Tumor Tissue Processing

Tumor tissue aliquots are collected during neurosurgical resection or biopsy. Tumor tissue was microdissected and suspended in RNAlater (Ambion) or flash-frozen, and stored at -80°C.

Total RNA Isolation

Frozen tissue was thawed and lysed in 1-2 mL of ice-cold TriZol Reagent (ThermoFisher Scientific, Cambridge, MA, USA). Lysate was homogenized by passing through a 20-gauge RNAse-free needle 10 times. Total RNA was then extracted as per the manufacturer's protocol and eluted in nuclease free water (Invitrogen). Both RNA quantity and quality were assessed for purity with Nanodrop One spectrophotometer (ThermoFisher Scientific, Cambridge, MA, USA). Agilent RNA 6000 pico kit was used with Agilent Technologies 2100 Bioanalyzer (Waldbronn, Germany) to determine the concentration and RIN (RNA Integrity Number) value of the samples.

Ethanol precipitation

To remove potential contaminants and carry-over inhibitors purification via ethanol precipitation was performed at multiple stages of the workflow: post extraction, post demethylation, and post poly(A)+ enrichment. To do this RNA was combined with 0.1 volume of 3 M, pH 5.2 sodium acetate and 3 volumes of ice-cold, 100% molecular biology grade ethanol (Sigma-Aldrich, St. Louis, MO). The ethanolic solution was stored at -20 ℃ overnight. Following this, RNA was recovered by centrifugation at 16,000g for 30 min at 4 ℃. The supernatant was carefully aspirated without disturbing the pellet. Subsequently, the pellet was washed with 0.5 ml of ice-cold, freshly prepared 70% ethanol. This was followed by centrifugation at maximum speed for 10 min at 4 ℃. The supernatant was removed and the tube was left open at room temperature to ensure that last traces of fluid have evaporated. The pellet was then dissolved and resuspended in nuclease free water (Invitrogen).

Enzymatic Demethylation

Total RNA extracted from each tumor tissue was equally split into two aliquots for subsequent demethylation or mock treatment. Given the variability in RNA yield from each tissue sample, up to 200 µg of RNA was either demethylated or mock treated with active recombinant FTO/ALKBH5 protein (Abcam, Cambridge) at a 1:0.3 molar ratio in a 500 µL reaction, as previously described by Zheng et. al, in 50 mM HEPES (Sigma-Aldrich, St. Louis, MO), 100 µM 2-oxoglutarate (Sigma-Aldrich, St. Louis, MO), 100 µM ascorbate (Sigma-Aldrich, St. Louis, MO), 50 µM Ammonium (II) Iron Sulfate (Sigma-Aldrich, St. Louis, MO), 1 mM TCEP (Sigma-Aldrich, St. Louis, MO), and 50 U of RNAse-Inhibitor (ThermoFisher Scientific, Cambridge, MA, USA)[35]. Care was taken to avoid

introduction of RNAses, and all solutions were prepared in nuclease free water (Ambion). RNA was ethanol precipitated and eluted in 100 µL of nuclease free water.

m^{6}A Quantification (ELISA)

Enzymatically demethylated and mock treated total or poly(A)+ RNA was assessed for integrity and concentration using RNA Pico Total RNA Assay and RNA Pico mRNA Assay (Agilent). 8 µL of RNA sample was used as input for the m^{6}A colorimetric assay (Abcam). Absorbance values at 450 nm and quantity of RNA from BioAnalyzer were used to calculate relative m^{6}A abundance (% m^{6}A). Efficiency of demethylation was quantified using the following equation: % m^{6}A demethylation = (Demethylated m^{6}A abundance/Mock m^{6}A abundance).

Poly(A)+ Isolation

Post enzymatic treatment with ALKBH5 or mock treatment, RNA samples were enriched for poly(A)+ species using the NEBNext® Poly(A) mRNA Magnetic Isolation Module (New England Biolabs,Ipswich, MA), according to manufacturer recommendations. All enrichment reactions were scaled up according to input RNA quantity, using 5 µg as upper limit for individual samples. Eluted poly(A)+ RNA was then assessed for quality and concentration by the RNA Pico mRNA Assay (Agilent).

Library Preparation and Sequencing

Demethylated and mock treated poly(A)+ RNA from NEBNext poly(A) isolation module (New England Biolabs) was eluted according to manufacturer's instructions, and then ethanol precipitated. RNA was pelleted and resuspended in 10 µL of nuclease free water (Invitrogen). 1 µL was used for RNA Pico mRNA Assay for quality check. The remaining 9 µL was used as input for library preparation. Libraries were prepared using the SQK-RNA002 kit (Oxford Nanopore Technologies) with selected modifications based on previous optimization runs: RTA and RMX ligation times were extended to 25 minutes, elution times were extended to 15 minutes, bead-binding times on Hula mixer were extended to 7 minutes, and Superscript IV (ThermoFisher Scientific) was used instead of Superscript III (ThermoFisher Scientific). As such, thermocycling conditions were modified, and the RTA adapted RNA was reverse transcribed at 53°C for 50 minutes, with reaction inactivation at 80°C for 10 minutes, before holding at 4°C. Following library preparation, demethylated and mock treated poly(A)+ RNA samples were sequenced on a MinION sequencer using R9 flow cells (Oxford Nanopore Technologies) for 24 hours, or until refuel of flow cell resulted in a lack of reads. Live basecalling (fast) was used to monitor Q-score (Qfilter ≥ 5) and translocation speed for the purposes of refueling.

Statistical analysis

Raw Sequencing throughput, QC, Genome Alignment, and Quantification

Total RNA extracted from each patient tissue sample was split into two aliquots, demethylated along with a mock control, and sequenced in parallel. Raw FAST5 files were compiled for each sequencing run, and pass reads (qscore>7) were basecalled using Dorado (0.5.0+0d932c0) using the model *rna002_70ps_fast@v3*. The resulting FASTQ files were processed using *nanoseq* (3.1.0) (https://github.com/nf-core/nanoseq/tree/dev), an analysis pipeline for Direct RNA Sequencing Data. It comprises raw read QC, alignment, and quantification.

During the first part of *nanoseq*, QC metrics from raw reads were generated using *Nanoplot*. Next, reads were aligned to the human (GRCh38) genome using minimap2 (2.17-r941). Post alignment, SAM files were converted to sorted BAM files using *samtools* (1.16.1) and mapping metrics were

presented using *MultiQC* (1.11). Finally, *nanoseq* utilized *bambu* (3.0.8) to quantify human genome alignments and generate gene counts and normalized abundances. The resulting raw count data were imported into R for differential expression analysis.

Full Length Reads

Reads counts mapped as full length reads for each transcript were estimated using *Bambu* (3.7.0).

Differential expression and isoform usage analysis

We used *DESeq2* (1.45.3) in R to test for differential gene and isoform expression between the two IDH1 groups and three classification groups. First, lowly expressed genes were filtered out by removing genes with less than 10 counts across all samples. The remaining counts were normalized using DESeq's internal size factor estimation. Log2 fold changes and adjusted p-values (Benjamini-Hochberg) were calculated, with an adjusted p-value (FDR) threshold of 0.05. For isoform-level differential expression, isoform counts were generated using *NanoCount* (1.0.0.post6) and were similarly processed using DESeq2. The isoform-level results were obtained by applying the same normalization, model fitting, and statistical testing procedures as described for genes. Differential isoform usage analysis was performed in R using IsoformSwitchAnalyzeR (2.5.0). The isoform counts and abundances were input along with the annotation and transcriptome files. Single isoform genes were filtered out during the *preFilter()* step since these genes cannot have changes in isoform usage. Statistical analysis was performed with *isoformSwitchTestSatuRn()*. We required a difference in isoform proportions between classification groups of >0.2 and an FDR-adjusted p-value of <0.05 for significance. The functional consequences of the identified isoform switches were generated using the analyzeSwitchConsequences() function. This analysis identified changes in important function domains such as coding potential, exon loss, domain loss, and isoform length.

Transcriptome-wide m6A modification sites

We used m6anet (2.1.0), a machine learning-based tool, to detect m6A sites in DRACH motifs from our direct RNA reads in all samples. Input data included raw nanopore FAST5 reads, which were aligned to the reference genome using minimap2. After alignment, m6ANet was employed to predict m6A modification sites based on sequence context and nanopore signal patterns. The output of m6anet provided predicted m6A sites with probability that the site is modified, the transcript position of the site, the 5-mer motif of the site, and the estimated percentage of reads in the site that is modified.

Distribution of modified sites

To analyze the distribution of m6A-modified sites across transcript regions, custom R scripts were used to calculate the lengths of the 5' UTR, CDS, and 3' UTR regions. For each transcript, the coding sequence (CDS) length was determined by summing exon lengths, while the UTR lengths were calculated based on start and end coordinates. Transcripts with missing UTR annotations were assigned a length of zero for the missing regions. To visualize the distribution of m6A-modified sites across these regions, a custom function was implemented in Python. The transcript position of each modification site was compared with the UTR and CDS regions to determine if the site was located within the 5' UTR, CDS, or 3' UTR. The relative position within each region was calculated, and kernel density estimation (KDE) plots were generated to visualize the relative density of m6A sites across these transcript regions. Modifications grouped by transcript biotypes (protein-coding, nonsense mediated decay, retained intron) and methylation status were visualized.

References

1. Miller, K. D. *et al.* Brain and other central nervous system tumor statistics, 2021. *CA Cancer J. Clin.* **71**, 381–406 (2021).
2. Ostrom, Q. T., Cote, D. J., Ascha, M., Kruchko, C. & Barnholtz-Sloan, J. S. Adult Glioma Incidence and Survival by Race or Ethnicity in the United States From 2000 to 2014. *JAMA Oncol* **4**, 1254–1262 (2018).
3. Yan, H. *et al.* IDH1 and IDH2 mutations in gliomas. *N. Engl. J. Med.* **360**, 765–773 (2009).
4. Dang, L. *et al.* Cancer-associated IDH1 mutations produce 2-hydroxyglutarate. *Nature* **462**, 739–744 (2009).
5. Nobusawa, S., Watanabe, T., Kleihues, P. & Ohgaki, H. IDH1 mutations as molecular signature and predictive factor of secondary glioblastomas. *Clin. Cancer Res.* **15**, 6002–6007 (2009).
6. Zou, P. *et al.* IDH1/IDH2 mutations define the prognosis and molecular profiles of patients with gliomas: a meta-analysis. *PLoS One* **8**, e68782 (2013).
7. Louis, D. N. *et al.* The 2021 WHO Classification of Tumors of the Central Nervous System: a summary. *Neuro. Oncol.* **23**, 1231–1251 (2021).
8. Alshiekh Nasany, R. & de la Fuente, M. I. Therapies for IDH-Mutant Gliomas. *Curr. Neurol. Neurosci. Rep.* **23**, 225–233 (2023).
9. Solomou, G., Finch, A., Asghar, A. & Bardella, C. Mutant IDH in Gliomas: Role in Cancer and Treatment Options. *Cancers* **15**, (2023).
10. Han, S. *et al.* IDH mutation in glioma: molecular mechanisms and potential therapeutic targets. *Br. J. Cancer* **122**, 1580–1589 (2020).
11. Ward, P. S. *et al.* Identification of additional IDH mutations associated with oncometabolite R(-)-2-hydroxyglutarate production. *Oncogene* **31**, 2491–2498 (2012).
12. Ward, P. S. *et al.* The common feature of leukemia-associated IDH1 and IDH2 mutations is a neomorphic enzyme activity converting alpha-ketoglutarate to 2-hydroxyglutarate. *Cancer Cell* **17**, 225–234 (2010).
13. Hurley, J. H., Dean, A. M., Koshland, D. E., Jr & Stroud, R. M. Catalytic mechanism of NADP(+)-dependent isocitrate dehydrogenase: implications from the structures of magnesium-isocitrate and NADP+ complexes. *Biochemistry* **30**, 8671–8678 (1991).
14. Natsumeda, M. *et al.* Accumulation of 2-hydroxyglutarate in gliomas correlates with survival: a study by 3.0-tesla magnetic resonance spectroscopy. *Acta Neuropathol Commun* **2**, 158 (2014).
15. Du, X. & Hu, H. The Roles of 2-Hydroxyglutarate. *Front Cell Dev Biol* **9**, 651317 (2021).
16. Elkashef, S. M. *et al.* IDH Mutation, Competitive Inhibition of FTO, and RNA Methylation. *Cancer Cell* **31**, 619–620 (2017).
17. Unruh, D. *et al.* Methylation and transcription patterns are distinct in IDH mutant gliomas compared to other IDH mutant cancers. *Sci. Rep.* **9**, 8946 (2019).
18. Körtel, N. *The Role of M6A RNA Modification in Post-Transcriptional Regulation of Gene Expression*. (2023).
19. Arzumanian, V. A., Dolgalev, G. V., Kurbatov, I. Y., Kiseleva, O. I. & Poverennaya, E. V. Epitranscriptome: Review of top 25 most-studied RNA modifications. *Int. J. Mol. Sci.* **23**, 13851 (2022).
20. Jiang, X. *et al.* The role of m6A modification in the biological functions and diseases. *Signal*

Transduct Target Ther **6**, 74 (2021).
21. Huang, W. *et al.* N6-methyladenosine methyltransferases: functions, regulation, and clinical potential. *J. Hematol. Oncol.* **14**, 117 (2021).
22. Chen, Y. *et al.* Context-aware transcript quantification from long-read RNA-seq data with Bambu. *Nat. Methods* **20**, 1187–1195 (2023).
23. Hendra, C. *et al.* Detection of m6A from direct RNA sequencing using a multiple instance learning framework. *Nat. Methods* **19**, 1590–1598 (2022).
24. Vitting-Seerup, K. & Sandelin, A. IsoformSwitchAnalyzeR: analysis of changes in genome-wide patterns of alternative splicing and its functional consequences. *Bioinformatics* **35**, 4469–4471 (2019).
25. Vogel, F. C. E., Chaves-Filho, A. B. & Schulze, A. Lipids as mediators of cancer progression and metastasis. *Nat Cancer* **5**, 16–29 (2024).
26. Dowdy, T. *et al.* Sphingolipid Pathway as a Source of Vulnerability in IDH1 Glioma. *Cancers* **12**, (2020).
27. Wojnacki, J. *et al.* Role of VAMP7-Dependent Secretion of Reticulon 3 in Neurite Growth. *Cell Rep.* **33**, 108536 (2020).
28. Amankulor, N. M. *et al.* Mutant IDH1 regulates the tumor-associated immune system in gliomas. *Genes Dev.* **31**, 774–786 (2017).
29. Kohanbash, G. *et al.* Isocitrate dehydrogenase mutations suppress STAT1 and CD8+ T cell accumulation in gliomas. *J. Clin. Invest.* **127**, 1425–1437 (2017).
30. Lucena-Cacace, A., Otero-Albiol, D., Jiménez-García, M. P., Peinado-Serrano, J. & Carnero, A. NAMPT overexpression induces cancer stemness and defines a novel tumor signature for glioma prognosis. *Oncotarget* **8**, 99514–99530 (2017).
31. Yavuz, B. B., Kilinc, F., Kanyilmaz, G. & Aktan, M. Pyruvate kinase M2 (PKM-2) expression and prognostic significance in glioblastoma patients. *J. Neurooncol.* **165**, 527–533 (2023).
32. Karakulak, T., Moch, H., von Mering, C. & Kahraman, A. Probing Isoform Switching Events in Various Cancer Types: Lessons From Pan-Cancer Studies. *Front Mol Biosci* **8**, 726902 (2021).
33. Bledea, R. *et al.* Functional and topographic effects on DNA methylation in IDH1/2 mutant cancers. *Sci. Rep.* **9**, 16830 (2019).
34. Pianka, S. T. *et al.* D-2-HG Inhibits IDH1mut Glioma Growth via FTO Inhibition and Resultant m6A Hypermethylation. *Cancer Res Commun* **4**, 876–894 (2024).
35. Zheng, G. *et al.* ALKBH5 is a mammalian RNA demethylase that impacts RNA metabolism and mouse fertility. *Mol. Cell* **49**, 18–29 (2013).
36. Dorado. https://github.com/nanoporetech/dorado
37. NanoPlot. https://github.com/wdecoster/NanoPlot
38. Li, Heng. Minimap2: pairwise alignment for nucleotide sequences. *Bioinformatics* **34**, 3094–3100 (2018).
39. Li, Heng. *et al.* The Sequence Alignment/Map format and SAMtools. *Bioinformatics* **25,** 2078–2079 (2009).
40. Ewels, Philip. *et al.* MultiQC: summarize analysis results for multiple tools and samples in a single report. *Bioinformatics* **32**, 3047–3048 (2016).
41. Chen, Y. *et al.* Context-aware transcript quantification from long-read RNA-seq data with Bambu. Nat Methods **20**, 1187–1195 (2023).
42. Love, M.I., Huber, W. & Anders, S. Moderated estimation of fold change and dispersion for RNA-seq data with DESeq2. Genome Biol **15**, 550 (2014).
43. Gleeson, Josie. *et al.* Accurate expression quantification from nanopore direct RNA sequencing with NanoCount, Nucleic Acids Research **50**, e19 (2022).
44. Vitting-Seerup, K., Sandelin A. IsoformSwitchAnalyzeR: analysis of changes in genome-wide patterns of alternative splicing and its functional consequences. Bioinformatics **35,** 4469-4471 (2019).

Figure Legends

Figure 1. Overview of m^{6}A Direct RNA Sequencing Approach. (a) Schematic showing RNA extraction and RNA preparation upstream of library preparation. RNA from tumor tissue with patients from glioma (n=15) is extracted using TriZol Reagent. RNA is either mock treated, or demethylated using recombinant ALKBH5. Both control and demethylated RNA are evaluated again for quality, and then enriched for the transcriptome using oligod(T) beads. Library preparation was conducted using direct RNA Sequencing (SQK-RNA002) protocol. Parallel sequencing of ALKBH5 treated and untreated samples performed using MinION. (b) Stacked bar graphs demonstrating the percentage of mapped and unmapped reads from ALKBH5 treated (left) and untreated (right) RNA isolated from IDH mutant (P1-P8, n = 8) and IDH wild-type (P9-P15, n = 7) glioma tumor tissue. (c) Venn Diagram (top) comparing the number of common and unique genes detected in all ALKBH5 treated (n = 15) and untreated (n = 15) samples. Dot plot (bottom) comparing the average quality score of the sequencing output from treated and untreated RNA in individual patients. (d) Quality control (QC) Nanoplots plotting log transformed read length vs average read quality (using a kernel density estimate) in ALKBH5 treated (n = 15, left) and untreated (n = 15, right) samples. (e) Weighted histogram of read lengths after log transformation in ALKBH5 treated (top) and untreated (bottom) samples.

Figure 2. Quantification of RNA biotypes and full-length transcripts across clinical groups. (a) Stacked bar graph demonstrating the relative abundance of protein coding, mitochondrial RNA (Mt RNA) and other biotypes across individual patients (n = 15). (b) Stacked bar graph demonstrating the relative abundance of other (lncRNA, pseudogenes, IG and TCR RNA, small RNA, ribozyme, rRNA) across individual patient. (n = 15). (c) Pie chart summarizing the relative abundance of RNA biotypes in the study cohort stratified by glioma subtype; astrocytoma (n = 6), oligodendroglioma (n = 2), and glioblastoma (GBM, n = 7). (d-i) Stacked plots comparing the prevalence (%) of full-length RNA transcripts of varying lengths (<500bp - >10,000bp) in different groups: (d) ALKBH5 treated vs untreated RNA, All (e) IDH mutant vs wild-type glioma, ALKBH5 untreated RNA, (f) IDH mutant vs wild-type glioma, ALKBH5 treated RNA, (g) ALKBH5 treated vs untreated RNA, Astrocytoma, (h) ALKBH5 treated vs untreated RNA, Oligodendroglioma, (i) ALKBH5 treated vs untreated RNA, Glioblastoma.

Figure 3. Differential gene expression analysis across glioma subtypes. (a-c) Heatmaps representing the top 200 differentially expressed genes for three comparisons: (a) IDH1 mutant vs wild-type, (b) astrocytoma vs glioblastoma (GBM), and (c) GBM vs oligodendroglioma. Gene expression levels are depicted by a color gradient, with red indicating upregulation and blue indicating downregulation. Rows represent individual genes, and column represent samples within each group. (d-f) Volcano plots highlighting significantly differentially expressed genes for the same comparisons as in panels a-c. Each point represents a gene, with log2 fold changes on the x-axis and -log10 adjusted p-values on the y-axis. Red dots correspond to significantly upregulated genes (adjusted p-value <.05, log2 fold change >1).

Figure 4. Clinically relevant genes exhibit different isoform usage between Astrocytoma and Glioblastoma (GBM). (a-p) Gene and isoform expression plots represented as bar graphs comparing gene expression (first), isoform expression (second), and isoform usage (third). Top panel shows the isoform structure with protein domains highlighted. Gene and isoform expression bar plots are shown below. (q) Consequences of isoform switch in astrocytoma vs GBM, comparing differences in the fraction of alternative splicing events. Data points denote fraction of genes having the consequence with size of the circle representing the number of genes and horizontal bar indicating 95% confidence interval. (r) Bar graphs depicting the number of isoform switching consequences associated with different glioma subtypes.

Figure 5. Deduction of m^{6}A consensus motifs and distribution and biotype analysis of m6A modifications across the mRNA transcriptome. (a) Consensus MOTIF definition of m^{6}A modifications in the transcriptome in IDH mutant (n = 8, left) and IDH wild-type (n = 7, right) glioma. Bitplot depicting the nucleotide composition with height of each symbol indicating the relative frequency of each nucleotide at that position. (b) Venn Diagrams comparing the number of common

and unique m^6A sites detected in IDH mutant vs wild-type glioma (left) and across the glioma subtypes (right). (c) Prevalence of m^6A RNA biotypes in IDH mutant (left) and wild-type (right) gliomas. (d) Metagenes plot depicting m^6A RNA mapping in a transcriptome pattern in individual patients (top, left). m^6A RNA mapping patterns in IDH mutant vs wild-type gliomas across different RNA biotypes: protein coding (top, right), retained intron (bottom, left), and nonsense mediated decay (bottom, right).

Figure 6. Chromosomal distribution analysis of m^6A sites across hallmark glioma alterations. (a-f) Stacked bar graphs denoting the number of m^6A sites detected per chromosome in the mutant (yellow) vs. wild-type (grey) groups stratified by glioma specific mutations: (a) IDH1, (b) ATRX, (c) MGMT, (d) EGFR, (e) TERT, (f) TP53.